PCCP

Accepted Manuscript

ARTICLE

Composition-Controlled Synthesis of Carbon-Supported Pt–Co Alloy Nanoparticles and Their Origin of the Activity Enhancement for Oxygen Reduction Reaction

Yige Zhao, Jingjun Liu*, Yanhui Zhao, Feng Wang**

The ability to precisely tune the chemical composition and the electronic structure in nanoalloy catalysts is essential for achieving the goal of high activity and selectivity for oxygen reduction reaction (ORR) on the catalysts by design. In this work, we synthesized carbon-supported Pt–Co alloy nanoparticles with controlled bimetallic compositions (Pt/Co atomic ratio = 81:19, 76:24, 59:41, 48:52, 40:60 and 26:74) by regulating pH of solutions and the amount of Pt and Co precursor salts to elucidate the effect of the composition of the catalysts on the ORR activity. The obtained Pt–Co alloy nanoparticles have a face-centred cubic (fcc) structure and are well dispersed on the surface of the carbon support with narrow particle size distribution (2~4 nm diameters). The electrocatalysis experiments in an alkaline solution reveal a strong correlation between the ORR activity and alloy composition for the alloy catalysts. Interestingly, the mass-specific activities of the catalysts manifest a typical double-volcano plot as a function of alloy compositions. In this Pt–Co alloy series, the catalyst with a Pt:Co atomic ratio of 76:24 exhibits the best ORR performance, which is remarkably higher than that of the commercial Pt/C (E-TEK). X-ray photoelectron spectroscopy (XPS) measurements demonstrate that the electronic structures for these catalysts could be tuned by controlling their alloy compositions, which are highly correlated with the trends in the ORR activity. The origin of the enhancement of the ORR activity may be substantially related to the unique chemical surface structures of the catalysts.

1. Introduction

One of the main challenges to be addressed for practical applications of low-temperature fuel cells, metal-air batteries, sewage advanced electro-oxidation treatment and chlor-alkali electrolysis is improving the activity of cathodic catalysts toward oxygen reduction reaction (ORR), because the ORR is a sluggish kinetics [1], which has been identified as a major impediment for a further development of these industrial fields above. To overcome the barrier, the development of highly active catalysts for the ORR is essential and urgent for us. By now, a great deal of efforts has been devoted to fabrication of highly active electro-catalytic catalysts. Although pure Pt has high activity toward the ORR, its high cost and poor stability make it difficult to further practical application[2]. Therefore, recent studies have aimed that Pt alloyed with a secondary metal (M=Co, Ni, Fe, Cr, Cu) may not only help to reduce the loading of precious Pt, but also allow the individual functional components to work synergistically to improve the catalytic performance, thus promising a much more flexible design of catalysts [3–6]. Among the bimetallic catalysts above, Pt–Co

systems have become a hot research topic and considerable advances have been made in the development of high active Pt–based bimetallic catalysts.

To date, many synthesis strategies for Pt-based bimetallic catalysts have been proposed in the literatures [7]: (i) colloidal chemistry method (ii) impregnation method (iii) polyol method. Among the methods mentioned above, the polyol process is a classical and promising synthesis method to prepare binary Pt-based alloy catalysts. In a typical polyol process, metallic compounds are either dissolved or suspended in ethylene glycol or diethylene glycol. The mixture is heated to a temperature which can reach the boiling point of the diol, subsequently resulting in the co-reduction of the metal salts and precipitation of bimetallic particles. Advantages of this method are that the as-synthesized catalysts possess control of particle size and size distribution, high dispersion on the supports and precisely tunable bimetallic composition. The ability of the polyol synthesis to precisely tune the chemical composition and particle sizes in nanoalloy catalysts make it become the most effective and widely used approach to metal nanoparticles [4].

By now, compared to the commercial Pt/C catalyst(E-TEK), the improved ORR kinetics for various Pt–M/C alloy catalysts have been observed, but the precise origins of the ORR activity on these catalysts have remained particularly elusive because little work has been done to systematically correlate the nature of the relevant electrocatalytic performance with a broad range of chemical compositions in these alloy nanoparticles.

Early results have shown that the enhancement of electrocatalytic oxygen reduction performance results from some factors such as changes in Pt−Pt interatomic distances, the electronic structure, Pt skin effect, etc [1,8]. In fact, the these structural changes can be achieved by manipulating the alloy composition in a wide range and the resulting shrinking of interatomic distances and d-band center shift that are responsible to the enhanced catalytic activity toward the ORR for most existing Pt-based bimetallic catalysts. Christopher Koenigsmann [8] confirmed that highly active catalysts have also been prepared by rationally manipulating the chemical composition so as to manipulate their corresponding electronic properties for Pt-based bimetallic catalysts involved homogeneous alloy-type formulations, hierarchical core-shell structures. A further examination of the electrocatalysis data for the ORR on Pt-based catalysts reveal that the alloy nanoparticles with an appropriate foreign metal content could provide a synergistic catalytic effect that involves breaking the O=O bond and reducing the resulting adsorbed atomic oxygen (suppression of adsorbed poisonous species), except for the change in electronic band structure to enhance the activity for ORR [9]. So, controlling the chemical composition besides particle size and phase structures of Pt-based catalysts is of primary importance in the fine-tuning of electronic effect and geometric effect, and in turn, in improving their ORR efficiencies. The understanding of electronic effect and geometric structures of the catalysts is essential for the exploitation of the enhanced ORR kinetics for bimetallic and multimetallic nanoparticles in catalytic reactions.

Herein, we synthesized carbon-supported Pt–Co alloy nanoparticles over a wide range of bimetallic compositions (Pt/Co atomic ratio = 81:19, 76:24, 59:41, 48:52, 40:60 and 26:74) by regulating the pH value and the amount of Co precursor to elucidate the effect of the composition of nanocatalysts on the ORR activity. The synthesis uses ethylene glycol as solvent and stabilizing agent. Changing the pH of such polyol solution gives freedom of the final particle sizes and compositions[10-11]. The composition-dependent enhancements of electrocatalytic oxygen reduction performance for Pt–Co bimetallic catalysts in alkaline solutions were characterized using rotating disk electrode and Tafel plots techniques. XPS measurements on the as-synthesized catalysts were carried out in order to investigate the effects of the unique electronic structures of the Pt–Co catalysts on the improved activity toward the ORR kinetics. The aim is to gain insights into the intrinsic correlation between the relevant enhanced activity and chemical compositions in these alloy catalysts. This information is important for the understanding of the physical origin of the activity and selectivity of the Pt–Co alloy catalysts during the ORR.
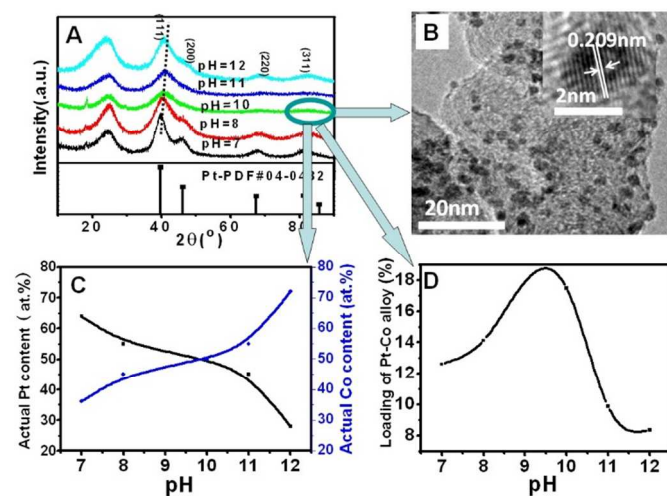
2. Experimental

We synthesized a wide composition range of Pt–Co bimetallic nanoparticles supported on the carbon black (Pt–Co/C) in a modified polyol system containing $NaBH_4$ as reducing agents. The alloyed Pt–Co/C catalysts over a wide range of bimetallic composition (Pt/Co atomic ratio = 81:19, 76:24, 59:41, 48:52, 40:60 and 26:74) were synthesized by regulating the pH value and the concentrations of H_2PtCl_6 and $CoCl_2$ in solutions containing carbon black support at 80 ℃. In a typical synthesis process, initially, 100 mg of the carbon black (Vulcan XC–72) was placed in 50 ml of ethylene glycol (EG) and sonicated for 20 min. Secondly, EG solution of H_2PtCl_6 (0.01M) and aqueous solution of $CoCl_2$ (0.1M) were prepared and then added to the carbon black suspension, followed by the adding of aqueous solution of NaOH (1M) into the mixture until the solution pH was adjusted. After stirring for 30 min, the resultant solution was heated to 80 ℃, then 20 ml $NaBH_4$ (1.89M) was added drop into the solution and the mixture was heated at 80 ℃ for 3 h with constant stirring. Afterward, the reaction mixture was washed several times by centrifugation, and then the obtained powder was dried at room temperature.

The structure and morphology of the synthesized Pt–Co/C samples were observed by powder X-ray diffraction (XRD) and transmission electron microscopy (TEM). The XRD characterization of the samples was performed with Cu KR radiation at λ=1.54 Å on a Philips Xpert X-ray diffractometer. TEM characterization of the samples was performed with a JEOL TEM 2010 microscope. The catalyst composition was obtained by ICP measurements. The samples were studied by an aberration-corrected scanning transmission electron microscope (STEM, JEOL ARM 200F) operated at 200kV and Energy Dispersive X-ray spectroscope (EDX) mapping . X-ray photoelectron spectra (XPS, ESCALAB 250) were obtained from a monochromator (Al KR source) calibrated with respect to the C (1s) peak at 284.6 eV. To study the electrocatalytic characteristics of our Pt–Co/C catalyst, a conventional three-electrode system was used at room temperature throughout this work. The electro-catalytic activity toward the ORR for the synthesized Pt–Co/C catalysts with different alloy compositions were characterized using rotating disk electrode and Tafel plots techniques in 1M NaOH solution, and were also compared with that obtained with the commercial Pt/C catalysts (E-TEK) under the same measurement conditions. During the electrochemical measurements, the rotating ring-disk electrode (RRDE) was used as working electrode. The counter electrode was Pt foil, and a saturated calomel electrode (SCE) was used as reference electrode, respectively. To prepare the working electrode, 10 mg of Pt–Co/C catalysts or Pt/C catalysts was dispersed ultrasonically in 2mL of alcohol and 100μL of Nafion. Then, 10μL of the Pt–Co/C or Pt/C suspension was pipetted onto ring rotating disk electrode (S=0.247cm^2). All of the scan rate is 5 mV/s.

2 | *Phys. Chem. Chem. Phys.*, 2014, **00**, 1-3

This journal is © The Royal Society of Chemistry 2014

3. Results and discussion

### 3.1 The pH–effect on formation of Pt–Co alloy nanoparticles

Figure 1. Effect of pH values of solutions on the crystalline structure, particle size, composition and loading for carbon-supported Pt–Co bimetallic nanoparticles with the fixed synthetic feeding (Pt:Co atomic ratio of 1:1) and metal loading of 20 wt.% with respect to carbon support, **(A)** XRD patterns of Pt–Co/C samples; **(B)** TEM images of Pt–Co/C samples at the pH=10; **(C)** actual atomic ratio of Pt:Co; **(D)** actual loadings of Pt–Co/C samples.

To gain precise understanding impact of pH on the co-deposition processes of Pt and Co ions in the polyol solution containing $NaBH_4$ as reduction, we initially fabricated carbon-supported Pt–Co bimetallic nanoparticles in the solution with a fixed synthetic feeding (Pt:Co atomic ratio of 1:1). Figure 1A presents the XRD patterns for as-synthesized Pt–Co/C samples fabricated by varying the pH values of solutions. For these Pt–Co/C samples, the asymmetric peak of centered at $2\Theta = 25.2°$ corresponds to the C (0 0 2) plane; other four distinct diffraction peaks in the XRD pattern lines emerging at about 39°, 46°, 68°, and 81° can be ascribed to the planes (1 1 1), (2 0 0), (2 2 0) and (3 1 1) characteristic of the face-centered cubic (fcc) crystalline Pt, compared to those of pure Pt (JCPDS number: 04–0802). Moreover, these four diffraction peaks in these samples are slightly shifted to higher angles with respect to the corresponding peaks in pure Pt, indicating the alloy formation between Pt and Co. In Figure 1A, these diffraction peaks of Pt–Co alloys shifted to a higher angle direction along with the increase in pH, showing the alloying extent of Pt–Co alloys increase accordingly. Until the pH was 10, these diffraction peaks nearly have no longer shift obviously. At this pH, the obtained sample exhibits the widest diffraction peaks, suggesting the smallest particle size among all the samples. The formation of the particles involves the reduction of the Pt and Co precursor salts by the solvent, EG, which in return is oxidized. The oxidation of EG maybe result in glycolic acid or the glycolate anion, dependent on the synthesis solution pH. The glycolate anion acts a stabilizer for the alloy colloids and its concentration, and hence the resulting Pt–Co particle size, is controlled by the solution pH [10]. As evidenced from the high–resolution TEM image, the Pt–Co alloy nanoparticles present

good dispersion on carbon support (Figure 1B) and the particle size is ca. 2.3 nm (inset in Figure 1B). To further identify the effect of pH on alloy compositions of Pt–Co nanoparticles, the relationship between the synthetic feeding and the actual compositions of the alloy were compared. Figure 1C shows Pt and Co contents in the synthesized nanoparticles versus pH value profiles at a given feeding composition (Pt:Co atomic ratio of 1:1). It can be seen that Pt content in the alloys always decreases with the pH increasing from 7 to 12, while Co content increases accordingly (Figure 1C). It is evident that Pt preferentially deposited on the carbon support at the low pH regions, while Co does at the high pH regions. At the given pH of 10, the measured actual composition of the synthesized alloy is nearly close to the feeding composition (Pt:Co=1:1) via co-reduction of two metals. Besides the alloy composition, the pH also exhibits remarkable impact on the alloy loadings, as shown in Figure 1D. The loadings of the synthesized Pt–Co catalysts firstly increase and then decrease with the pH increasing from 7 to 12. Interestingly, a volcano-type dependence of alloy loadings for the nanoparticles on pH values was observed in Figure 1D. When the pH was justified to about 10 with sodium hydroxide, the highest alloy loading was obtained, which is nearly close to the theoretical metal loading (20 wt.%). This phenomenon is due to the variation of glycolate, the stabilizer of synthesis system. As pH increases, the amount of glycolate increases accordingly, the metals reduced keep the upward tendency, so that the metal loading grow correspondingly [10]. With further increase of pH, however, the stability of reducing agent ethylene glycol decreases, until losing the ability of reducibility, resulting in the decline of the loading. These outcomes clearly illustrate that the particle size, alloy composition and loading for the Pt–Co nanoparticles supported on carbon substantially depend on the pH of solutions. Therefore, controlling the pH values of solutions is of primary importance to tunable synthesis Pt–Co/C hybrid catalyst in the polyol solutions.

3.2 Tuning of alloy compositions of Pt–Co/C catalysts
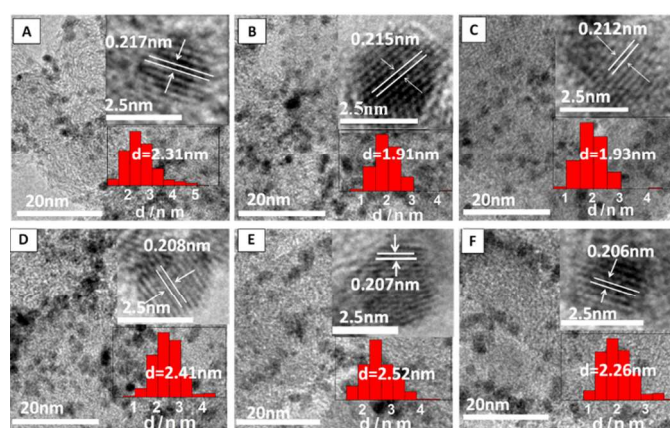
Figure 2. TEM images of Pt–Co/C catalysts with different bimetallic composition at a fixed metal loading of 20wt.%, prepared in the ethylene glycol solutions at

This journal is © The Royal Society of Chemistry 2014

Phys. Chem. Chem. Phys., 2014, **00**, 1-3 | **3**

80°C(pH = 10), **(A)** $Pt_{81}Co_{19}$; **(B)** $Pt_{76}Co_{24}$; **(C)** $Pt_{59}Co_{41}$; **(D)** $Pt_{48}Co_{52}$; **(E)** $Pt_{40}Co_{60}$; **(F)** $Pt_{26}Co_{74}$ (Insert: HRTEM images and the size distribution of Pt–Co alloy nanoparticles)

At the optimized pH of 10, a variety of Pt–Co naoparticles with a wide range of composition can have been successfully synthesized here. The chemical compositions of these alloy catalysts are shown to be effectively controllable in the range of Pt content from 24 at.% to 81 at.%, by manipulating the relative atomic ratios of Pt:Co in synthetic feeding in solutions. The samples of " $Pt_{81}Co_{19}$ 、 $Pt_{76}Co_{24}$ 、 $Pt_{59}Co_{41}$ 、 $Pt_{48}Co_{52}$ 、 $Pt_{40}Co_{60}$ 、 $Pt_{26}Co_{74}$ " referred in Figure 2 were prepared at the feeding composition of " 4:1、 3:1、 2:1、 1:1、 1:2、 1:3" at pH of 10, respectively, which demonstrates that " at the given pH of 10, the measured actual composition of the synthesized alloy is nearly close to the feeding composition" is applicable for other feeding composition. The atom percentage of Pt in the Pt–Co nanodendrites was determined by inductively coupled plasma (ICP) measurements. Figure 2 shows six typical TEM images of the Pt–Co/C catalysts with different compositions and their corresponding particle size distribution histograms. The Pt–Co alloy nanoparticles are found to be well-dispersed on the surface of carbon support with a narrow particle size distribution; the alloy nanoparticles are generally spherical in shape without agglomerates observed sporadically. Based on measuring the size of the chosen nanoparticles in the TEM images (the insets in Figure 2), the derived mean particle sizes of these Pt–Co nanoparticles with the increase in Pt contents are about 2.31, 1.91, 1.93, 2.41, 2.52 and 2.26 nm, respectively.

Figure 3A shows the XRD patterns of the carbon-supported Pt–Co particles over a wide range of bimetallic composition. The first peak located at 24.8° in all the XRD patterns except for the curve (a) is ascribed to the (0 0 2) plane of carbon support. The other four peaks can be ascribed to the planes (1 1 1), (2 0 0), (2 2 0) and (3 1 1) characteristic of the face-centered cubic (fcc) crystalline Pt, compared to those of pure Pt (JCPDS number: 04-0802). All the recorded diffraction peaks in the patterns of all the Co–Pt samples positioned between the reflections of pure Co and pure Pt, revealing the formation of Co–Pt alloy in Figure 3A. No peak for pure Co and its oxides was found in Figure 3A. This further indicates that all the Pt–Co nanoparticles are well-alloyed and they are principally single-phase solid solutions alloys. With an increase in the contents of Co atoms, these diffraction peaks of these alloy catalysts shifted to higher angles as compared to those of pure Pt. This indicates the contraction of the lattice due to substitution of Pt with Co atoms, which are smaller than Pt. As evidenced from the high-resolution TEM image (the insets in Figure 2), the particles were crystalline and the interplanar spacings (i.e., d-spacing) for these catalysts with different alloy compositions were less than 0.23 nm, which is the reported value of the (111) plane of cubic Pt.

Since the alloying is a key structural parameter related to ORR activity for the synthesized Pt–Co alloys [12] , we have, therefore, investigated the correlation between the lattice constants and Pt/Co atomic fractions of the alloy nanoparticles.

Figure 3B shows the calculated fcc lattice constants of Pt–Co nanoparticles from Figure 3A versus the Pt/Co atomic fractions. The dependence of fcc lattice constants on Co contents in the alloys is represented by the black line, while the theoretical dependence of the lattice parameter on Co contents is represented by the redline. It is obviously seen that the lattice constants linearly decreased with the increase of Co atomic fractions for these alloy samples. The results display the formation of the well-alloyed Pt–Co nanoparticles with a homogeneous solid-solution structure.
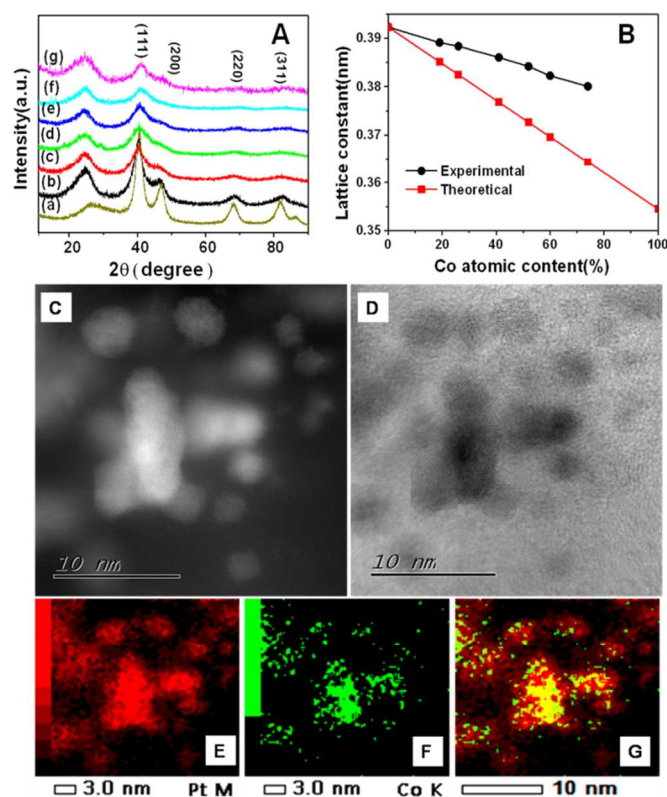
Figure 3. (A) X-ray diffraction patterns (XRD) for Pt–Co/C catalysts with different alloy compositions, (a) commercialPt; (b) $Pt_{81}Co_{19}$; (c) $Pt_{76}Co_{24}$; (d) $Pt_{59}Co_{41}$; (e) $Pt_{48}Co_{52}$; (f) $Pt_{40}Co_{60}$; (g) $Pt_{26}Co_{74}$; **(B)** The calculated fcc lattice constants of carbon-supported Pt–Co nanoparticles from the XRD analysis (Figure 3A) versus actual Co contents; **(C)** Annular dark-field STEM (ADF-STEM) and **(D)** BF-STEM overview images of the $Pt_{76}Co_{24}$ nanoparticle; **(E)-(G)** Energy-dispersive X-ray (EDX) mapping of Pt **(E)**, Co **(F)** along with the composite Pt versus Co map **(G)** .

To further confirm the alloying degree of the alloy, we have also evaluated the atomic level distribution of Pt and Co in the particles, represented by the as-prepared $Pt_{76}Co_{24}$ sample, employing the STEM images and EDX mapping. An ADF-STEM and BF-STEM overview images of $Pt_{76}Co_{24}$ alloy are shown in Figure 3C, D. The Pt and Co elements projected distributions within the particle are shown in Figure 3E, F. The Pt (red) versus Co (green) composite image (Figure 3G) indicates that the Pt and Co are uniformly distributed in the particle, further demonstrating the formation of Pt–Co alloy, which is consistent with our analysis in Figure 3B. Moreover, a slightly deviation between theoretical and experimental lines

4 | *Phys. Chem. Chem. Phys.*, 2014, **00**, 1-3

This journal is © The Royal Society of Chemistry 2014

has been observed in Figure 3B. If we don't consider the effect of the metal-carbon interaction, and assume that the dependence of the lattice parameter on Co contents is the same for supported and unsupported Pt–Co alloy nanoparticles, the deviation between theoretical and experimental lines presents the features of limited miscibility for Pt–Co alloy nanoparticles. Therefore, the synthesis of Pt–Co alloy nanoparticles with high alloying extent provides an opportunity to precisely evaluate the effects of the alloy compositions on their electrocatalytic activity for ORR in an alkaline solution.

3.3 Composition-effect on catalytic activity for ORR on Pt–Co/C catalysts

The correlation between the alloy compositions of these Pt–Co alloy catalysts and the electro-catalytic activity for the ORR was systematically investigated by using a rotating-disk electrode (RDE) in O_2-saturated 1 mol/L^{-1} NaOH solution at room temperature. Figure 4A shows a family of rotating disk voltammograms for these Pt–Co/C catalysts with different alloy compositions, at a fixed rotation of 1600 rpm. The result for the commercial Pt/C catalyst (E-TEK, 40 wt.% loading) is a reference material for comparison. For each catalyst, the measured current density (J) was normalized to loading amount of metal. Subsequently, the mass-transport corrected kinetically current densities (J_k) were obtained, by correcting the measured current density using the diffusion-limiting current density (J_L), according to the Koutecky-Levich equation [13]:

$$\frac{1}{J} = \frac{1}{J_k} + \frac{1}{J_L} \quad\quad （1）$$

Where J is the experimentally measured current from Figure 4A, J_L is the diffusion-limiting current, and J_k is the kinetic current. Then, the kinetic current was calculated based on the following equation:

$$J_k = \frac{J \times J_L}{J_L - J} \qu\quad （2）$$

The electro-catalytic activities of these catalysts, estimated from the onset potential, which was defined by the tangent method, follow the order $Pt_{76}Co_{24}$> $Pt_{81}Co_{19}$> $Pt_{59}Co_{41}$> $Pt_{48}Co_{52}$ > commercial Pt/C > $Pt_{40}Co_{60}$ > $Pt_{26}Co_{74}$, with the potential values of −0.092, −0.101, −0.110, −0.112, −0.115, −0.123 and −0.136V versus SCE in Figure 4B, respectively. Definitely, among all the tested Pt–Co/C catalysts, the $Pt_{76}Co_{24}$ catalyst exhibits the most positive onset potential, which is 23 mV higher than the commercial Pt/C catalyst. As regards the current activity, the mass-corrected ORR current densities at −0.15V in Figure 4C are compared in the order, $Pt_{76}Co_{24}$> $Pt_{81}Co_{19}$> $Pt_{59}Co_{41}$>$Pt_{48}Co_{52}$ > $Pt_{40}Co_{60}$> commercial Pt/C > $Pt_{26}Co_{74}$. As expected, the $Pt_{76}Co_{24}$ catalyst also exhibits the largest kinetic current density of 1.48 mA/cm^2, which is 1.85 times higher than that of the commercial Pt/C (E–TEK). This result is in good agreement with the results depicted by Figure 4B. These results illustrate that the ORR activity of the catalysts substantially depend on their alloy compositions.

To gain some insight into the origin of the activity enhancement for ORR, we plotted the mass–specific activities of Pt as a function of the alloy composition in this Pt–Co alloy series using the data in Figure 4C, as depicted from Figure 4D. It can be seen that all the Pt–Co/C catalysts with the Pt compositions from 40 at% to 81% exhibited better mass–specific activity than that of the commercial Pt/C catalyst. It illustrates that the alloying effect between Pt and Co atoms has a substantially impact on the ORR kinetics. Interestingly, the mass-specific activities for the synthesized Pt–Co/C catalysts reveals a double-volcano plot as a function of alloy composition, where the $Pt_{48}Co_{52}$ and $Pt_{76}Co_{24}$ catalysts locate at the peak positions respectively, as depicted from Figure 4D. The novel double-volcano-type curve is remarkably different from the accepted volcano-type correlation between the activity and alloy composition for other Pt–based catalysts [14-15].According to precious results reported in the literature [16], volcano-type relationship between the alloy compositions and their corresponding ORR activity are generally accepted in binary alloy systems and usually attributed to the changes in surface structures including geometric structure (ensemble effect) and electronic structure of Pt (electronic effect), which affect the ORR kinetics. To date, the exact origin of the activity enhancement for the Pt–Co/C catalysts is still a subject of ongoing discussion related to electronic and geometric structures for Pt-based bimetallic catalysts. In our case, the unique double-volcano feature in this Pt–Co alloy system could be attributed to the modification of electronic effect as a result of the alloying of Pt with Co element. A detailed electronic parameters analysis will be able to reveal the real nature of the catalysts responsible for the enhancement of ORR activity.
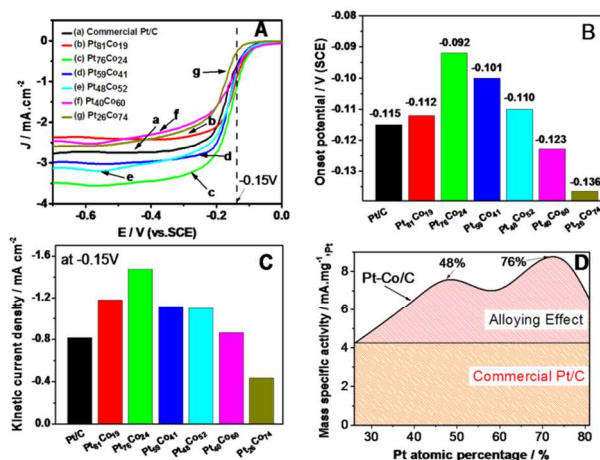

Figure 4. Rotating-disk electrode (RDE) measurements for ORR on Pt–Co/C catalysts with different alloy compositions in a 1 mol L^{-1} NaOH solution saturated with oxygen at room temperature; the scan rate was 10mV s^{-1}; the rotating speed was 1600 rpm. **(A)** cathodic polarization curves; **(B)** onset potentials; **(C)** the kinetic current densities at -0.15V; **(D)** the mass-specific activities of Pt as a function of the alloy composition.

So, we performed XPS experiments on the synthesized Pt–Co/C catalysts with different compositions and the resulting Pt 4f core–level binding energies were shown in Figure 5A.

This journal is © The Royal Society of Chemistry 2014

Phys. Chem. Chem. Phys., 2014, **00**, 1-3 | **5**

Analysis of the Pt 4f peaks with respect to the Pt/Co atomic ratios in Figure 5 shows that the Pt 4f peaks shift to lower binding energy with increasing the Co contents, suggesting that the electronic structure of the alloys were modified by the alloying of Pt with Co element. It is believed that changes in the d-band center accompany similar variations in the surface core-level shifts in the same direction [17]. So, the negative shift of the binding energy of the Pt 4f core level reflects the downshift of its d-band center relative Fermi level. According to the Hammer−Nørskov model, there is a close correlation between the d-band center of a metal surface and the ability to form chemisorption bonds [18]. As the d-band center shifts up, the chemisorption bond becomes increasingly stronger, while the chemisorption bond becomes weaker accordingly, as the d-band center shifts down. In our case, the downshifted d-band center in the Pt−Co catalysts would weaken the chemical adsorption strength of oxygenate intermediates such as OH_{ads} in alkaline solution, which would cause the Pt−OH_{ads} breaking easily and then lead to more electrochemically active sites available for the ORR. Unfortunately, in the other hand, the downshift of d-band center can also weaken the chemical adsorption strength of active oxygen and thus block subsequently O−O bond breaking, which deteriorate the ORR kinetics. Hence, regarding a counter balance between two opposite effects that are related to the adsorption strength of active oxygen and oxygenate intermediates (OH), there should be an optimum Pt 4f binding energy which is attributed to the best catalytic activity toward the ORR on the Pt−Co catalyst with appropriate alloy composition. However, a clearly tendency towards a linear downshift in Pt 4f binding energy with increasing the Co fraction in this Pt−Co series is obtained in Figure 5A, which is not in good agreement with the double-volcano-shaped trend in the ORR activity, as depicted by Figure 4D. It seems that the results in Figure 5A cannot reasonably explained the enhanced activity for the ORR catalyzed by the Pt–Co/C catalysts.

To further reveal the relationship of the electronic structures of the bimetallic catalysts and their ORR activity, we further fitted the XPS curves obtained in Figure 5A by using XSPEAK41 software. The fitted results were shown in Figure 5B and C. It can be seen that Pt in these catalysts contains various states such as Pt(0) (metallic Pt), Pt(II) (PtO), and Pt(IV) (PtO_2). Interestingly, an analogous double-volcano plot was observed, when the Pt^0 4f 7/2 or 4f 5/2 binding energies was plotted as a function of alloy compositions in Figure 5B and C, respectively. We compare the Pt(0) binding energies and mass specific activities on these catalysts against the Pt contents in the alloy catalysts in Figure 5B and C. It is evident that a nearly analogous correlation is observed between mass specific activities and zero covalent Pt(0) binding energies expressed as a function of the Pt content within the catalysts. Thereby, It strongly indicates that the changes in the Pt(0) core-level binding energy indeed affect the ORR kinetics. Among the alloy catalysts, the $Pt_{76}Co_{24}$ catalyst with the maximum ORR activity has a highest value of the binding energy of Pt(0) 4f, which is even higher that of the pure Pt (71.25 eV), as depicted

by Figure 5 B and C. For comparison, we further analyzed other Pt states besides the Pt(0) in the Pt−Co/C catalysts, and found that the obtained Pt(II) and Pt(IV) states exhibited similar double-volcano tendencies and matched the ORR kinetics well. Therefore, we concluded the enhanced activity toward the ORR on the catalyst with a certain alloy compositions substantially result from the unique electronic structure, which probably lead to more electrochemically active sites available for the ORR on the catalyst surface.
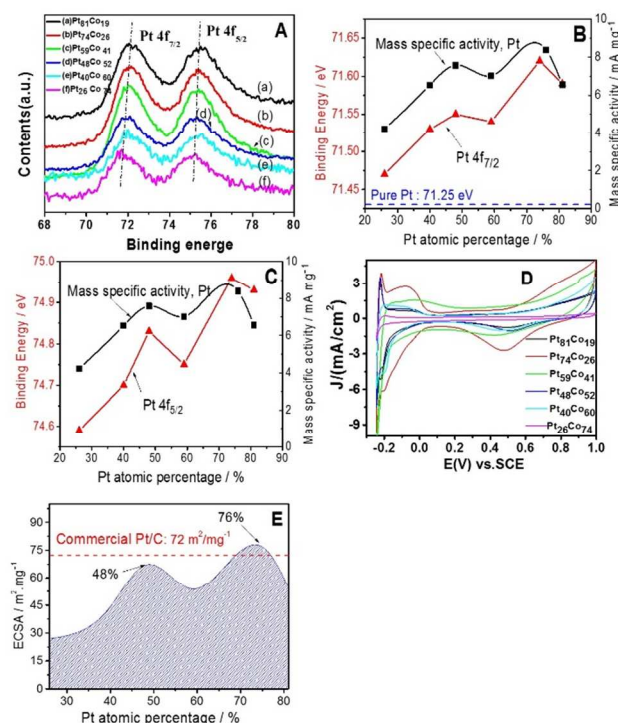
Figure 5. **(A)** XPS measurements on the synthesized Pt–Co catalysts with different alloy compositions; **(B)** double-volcano correlation between the fitted Pt(0) 4f 7/2 core-level binding energy and Pt atomic percentage; **(C)** double-volcano correlation between the fitted Pt(0) 4f 5/2 core-level binding energy and Pt atomic percentage; **(D)** CV curves for the synthesized Pt–Co catalysts with different alloy compositions recorded in an N_2-purged 0.5 M H_2SO_4 solution with a sweep rate of 50 mV/s; **(E)** the measured specific ECSA for the Pt–Co alloy catalysts and the commercial Pt/C (E-TEK).

To confirm this hypothesis, cyclic voltammetry(CV) curves for the synthesized Pt–Co/C catalysts were carried out in N_2–purged 0.5 M H_2SO_4 solution at a sweep rate of 50 mV/s and the results were shown in Figure 5D. The obtained CV curves exhibited two distinctive potential regions associated with H_{upd} adsorption/desorption processes between $-0.22 < E < 0V$, where H_{upd} refers to the under potentially deposited hydrogen species [19]. In Figure 5D, small shoulders characteristic of hydrogen adsorption on the Pt/C are also noticeable in the CV of the Pt–Co/C catalysts, but as the Co exceed 74 at% in the alloys, the features are lost and the total charge associated with hydrogen increases slightly. Subsequently, we calculated the electrochemically active surface area (ECSA) of these catalysts on the basis of the charge associated with the hydrogen desorption region after double-layer correction and assuming a

6 | *Phys. Chem. Chem. Phys.*, 2014, **00**, 1-3

This journal is © The Royal Society of Chemistry 2014

value of 210 μ C/cm^2 for the adsorption of a hydrogen monolayer [20]. In Figure 5E, it is noted that the recorded ECSA also present a double-volcano-type curve with respect to the Pt fractions in the Pt–Co alloy series, similar to the trend exhibited by the binding energies data of Pt (Figure 5 B and C). The result provides additional evidence that the unique electronic structures modulated by the bimetallic compositions can effectively modify the electrochemically active surface area for Pt–Co alloy catalysts, which facilitates the ORR kinetics. It is believed that the binding energies will affect the ECSA in some ways, but the mechanism of which needs further research.

3.4 Composition–dependent ORR kinetics on Pt–Co/C catalysts

To deeply understanding the ORR pathway via either a four–electron or a two-electron pathway on these Pt–Co/C catalysts with different compositions, we performed rotating ring-disk electrode (RRDE) measurements to monitor the number of transferred electrons (n) and the formation of peroxide species during the ORR in the 1M NaOH solution saturated with oxygen at room temperature. The ring and the disk currents in the negative sweep direction (5 mV s^{-1}) and at a constant ring potential of 0.5V (vs. SCE) were fixed in this case. At this ring potential, the oxidation of HO_2^-, which is produced at the disk electrode during the ORR, proceeds under pure diffusion control, while oxygen evolution currents at the Pt-ring are still negligible. Figure 6A compares the resulting disk and ring current results recorded at 1600 rpm for the Pt–Co alloy series. The result for the commercial Pt/C catalyst is a reference material for comparison. As expected, Figure 6A shows that the ring currents (I_r) are very low for these tested catalysts, compared to the corresponding disk currents (I_d). Among all the tested catalysts, the $Pt_{76}Co_{24}$ catalyst shows the highest disk current (O_2 reduction) and the smallest ring current (HO_2^- oxidation). It illustrates that the $Pt_{76}Co_{24}$ sample can effectively catalyze the ORR via a four–electron pathway, that is, a fast ORR kinetics, and then achieves the maximum ORR activity. The enhance electro-catalytic activity of $Pt_{76}Co_{24}$ catalyst over pure Pt and other Pt–Co catalysts are most likely due to the higher electrochemical specific area (Figure 5E).

To more clearly illustrate and visualize the correlation between the number of transferred electrons (n) and the alloy composition, we plotted the number of transferred electrons (n) as a function of the alloy compositions, as shown in Figure 6B. The number of transferred electrons involved in the ORR was calculated using equation (3), using the data in Figures 6A.

$$ n = 4 \frac{I_d}{I_d + I_r / N} \quad (3) $$

$$ HO_2^- = 200 \frac{\dfrac{I_r}{N}}{\dfrac{I_r}{N} + I_d} \quad (4) $$

Where, I_d is the disk current, I_r is the ring current, and N is the current collection efficiency of RRDE (0.37) [21]. In Figure 6B,

at a given polarization potential of –0.4V, the number of transferred electrons during the ORR reveals a double-volcano plot as a function of the alloy compositions within Pt–Co alloy series, where the $Pt_{48}Co_{52}$ and $Pt_{76}Co_{24}$ alloys locates at the peaks, respectively. The double-volcano-type correlation between the number of transferred electrons and the alloy composition in Figure 6B is similar to the trend exhibited by Pt(0) binding energy data (Figure 5B and C), thereby indicating that the ORR pathway is ascribed to the electronic structures of catalysts. Furthermore, in the Pt–Co alloy series, the $Pt_{76}Co_{24}$ catalyst exhibits the highest electron transfer numbers(3.99), which is also higher than that of the commercial Pt/C (3.95), further showing the ORR catalyzed by the catalyst follows a complete four-electron process leading to OH$^-$.
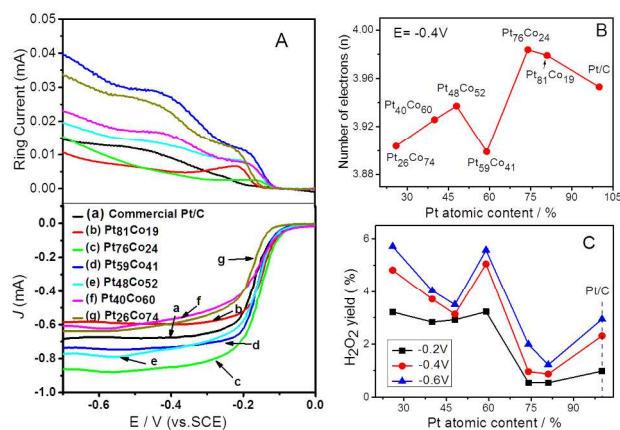

Figure 6. (**A**) Rotating ring-disk electrode voltammograms recorded on the synthesized Pt–Co catalysts and the commercial Pt/C in O$_2$-saturated 1 M NaOH at a rotation rate of 1600 rpm; the scan rate was 5 mV s^{-1} and the ring potential was constant at 0.5 V versus SCE (disk current is shown on the lower half and ring current is shown on the upper half of the graph); (**B**) the number of transferred electrons during ORR on the catalysts at a given polarization potential (–0.4V); (**C**) the hydrogen peroxide yields of the catalysts under different polarization potentials.

To better understanding the ORR kinetics, we further construct the correlation between hydrogen peroxide yields and the alloy composition under different cathodic polarization potentials, as shown in Figure 6C. The hydrogen peroxide yields generated during the ORR at the ring at 0.5 V was calculated using equation (4). The resulting peroxide formation against the alloy compositions reveal the inverse tendencies exhibited by the electron transfer numbers during the ORR, illustrating a strong correlation between hydrogen peroxide yields and the number of transferred electrons. For the Pt–Co alloy series, in Figure 6C, the $Pt_{76}Co_{24}$ catalyst shows the minimum peroxide yield during the ORR, which is slightly lower than that of the commercial Pt/C. The negligible hydrogen peroxide production further verifies that the ORR on the catalyst follows a fully four-electron process, a fast ORR kinetics, in the technically relevant potential region of –0.2 to –0.8 V (vs. SCE), which are desirable in terms of practical applications. Moreover, a close examination of the resulting hydrogen peroxide yields under different cathodic polarization potentials from –0.2V to –0.6V

revealed subtle differences, as shown in Figure 6D. It is noted that the peroxide yields slightly increase with increasing the employed polarization potentials in the negative direction, showing the strongly potential-effect on the peroxide formation in the alloy series. We attribute this increased peroxide yields to the strong formation of adsorbed oxygen species on catalyst surface at more negative polarization potentials, which reduces the probability for dissociative adsorption of O_2 and thus increases the probability for the nondissociative reduction of O_2 molecules and subsequent reduction to H_2O_2 [22]. This observation provides additional evidence that the origin of the selectivity of the Pt–Co alloy catalysts is affected by the alloy composition and thus related to the chemical surface structures of the catalysts.

In this work, Tafel plots for the Pt–Co/C catalysts were constructed by plotting the logarithm of the corrected kinetic current density (J_k) derived from the mass transport correction of the disk currents using data in Figure 4A. Figure 7A presents the obtained Tafel plots for the $Pt_{76}Co_{24}$ and commercial Pt/C catalysts. At first glance, the resultant plots present two well defined linear regions for both catalysts. We can see the Tafel slope at low overpotential region for two catalysts is very close to $-2.303RT/\alpha F \approx 60$ mV per decade (R, T, α and F are the molar gas constant, absolute temperature, transfer coefficient and Faraday constant, respectively), indicating the first electron transfer step catalysed by the Pt–Co alloy catalyst is probably the rate-determining step during the ORR. One is direct four-electron O_2 reduction, where first electron transfer is immediately followed by breaking of the O–O bond (no peroxide intermediates) [23]. In this case, the first-order dependence of the kinetics of the ORR is found [24]. In contrast, the Tafel slope at high overpotential region for the Pt/C and Pt–Co/C is very close to $-2.303 \times 2RT/\alpha F \approx 120$ mV per decade, illustrating the ORR processes controlled by the two-electron transfer step during the ORR. In this case, the ORR must be an indirection four-electron O_2 reduction that occurs in two steps: ① $O_2 + H_2O + 2e^- \rightarrow HO_2^-$ (slow) and ② $HO_2^- + H_2O + 2e^- \rightarrow 3OH^-$ (fast) and the former is the rate–determining step during the ORR [25]. It is evident that the change in Tafel slope implies a corresponding change in the rate determining step. The change in Tafel slope can be explained in terms of O_2 coverage: the Temkin isotherm (high O_2 coverage) at low overpotential region and the Langmuir isotherm (low O_2 coverage) at high overpotential region [26]. With increasing the overpotential, the rate of O_2 reduction decreases linearly with the surface coverage by reaction intermediates such as OH_{ads}, which control the availability of free adsorption sites for the adsorption of molecular O_2 and result in inhibition of the oxygen reduction reaction. In Figure 7B, the $Pt_{76}Co_{24}$/C catalyst exhibits the higher transition potential than that of the commercial Pt/C, showing the bigger breaking ability of the coverage dependent part of the either oxygen dissociation or the formation of the intermediates (OH) generated by ORR.

To gain the key kinetic parameters for the ORR on the catalysts, Tafel plots in Figure 7A were further fitted by using Tafel Equation (5):
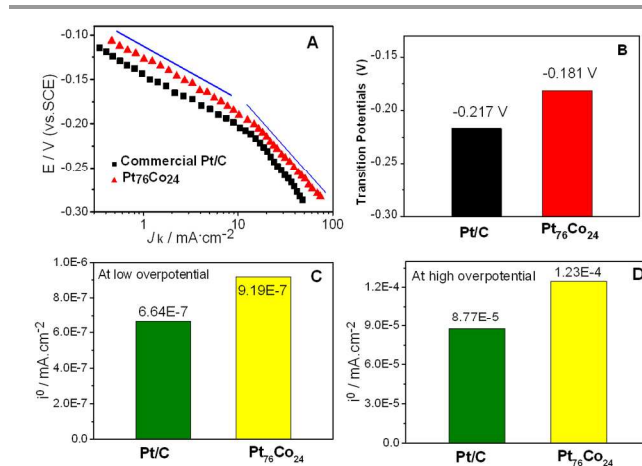
Figure 7. **(A)** Mass transport corrected Tafel plots for the ORR on RDE coated with $Pt_{76}Co_{24}$ and the commercial Pt/C catalysts in O_2-saturated 1M NaOH solutions. Scan rate: 5mV/s. Rotation speed:1600 rpm; **(B)** the transition potentials from the low overpotential region to the high overpotential region obtained from Figure 7A; **(C)** the exchange current density (i^0) obtained at low overpotential region; **(D)** the exchange current density (i^0) obtained at high overpotential region.

Table 1 Kinetic parameters of the ORR deduced from the Tafel slope for the $Pt_{76}Co_{24}$ catalyst and the commercial Pt/C at low and high overpotential regions, respectively.

Catalysts	At low overpotential region		At high overpotential region	
	b (V/dec)	i^0(mA/cm²)	b (V/dec)	i^0(mA/cm²)
Commercial Pt/C	−0.06037	6.64E-07	−0.11804	8.77E-05
$Pt_{76}Co_{24}$	−0.05998	9.19E-07	−0.1215	1.23E-04

$$E - E^0 = -b \lg i^0 + b \lg i \qquad (5)$$

Where E^0 is equilibrium potential of ORR; b is Tafel slope; and i^0 is exchange current density. The resulting kinetic parameters were given in Table 1. As expected, the exchange current densities for $Pt_{76}Co_{24}$ at both low and high overpotential regions are remarkably higher than those the Pt/C in Figure 7C and D. These outcomes verify that the optimum Pt–Co/C catalyst fabricated at the atomic ratio of 76:24 exhibits superior electro-catalytic activity toward the ORR in the alkaline solution, possibly as a result of the electronic effect. In addition, the exchange current density of $Pt_{76}Co_{24}$ catalyst obtained in the high overpotential region is remarkably higher than that obtained in the low overpotential region, revealing that the ORR kinetic rate is also significantly impacted by the potentials. The employed higher cathodic polarization potential will facilitate the ORR kinetics (the exchange current density), but the corresponding peroxide formation increase as a result of nondissociative reduction of O_2 molecules and subsequent reduction to H_2O_2 on the catalyst surface, as depicted by Figure 6D. Therefore, although the exact origin of the activity enhancement for the Pt–Co alloy catalysts is still a subject of ongoing discussion related to electronic (ligand) and geometric effects, it is clear that the kinetics enhancement in the ORR on

the Pt–Co alloy catalysts substantially depends on their electronic structures of the catalysts.

4. Conclusions

In this work, we synthesized carbon-supported Pt–Co bimetallic nanoparticles in a wide range of bimetallic composition by tuning pH of the solutions containing ethylene glycol and $NaBH_4$ as reducing agents. At a given pH of 10, the obtained Pt–Co bimetallic nanoparticles are well-alloyed and well dispersed on the surface of the carbon support with narrow particle size distribution (2~4 nm diameters). Electrocatalysis experiments in an alkaline solution showed that the alloying of Pt with Co could significantly improve the ORR activity and the improved ORR activity of the catalysts drastically depended on their compositions. The kinetic current density during the ORR on these Pt–Co alloy catalysts reveals a double-volcano plot as a function of alloy composition, where the $Pt_{48}Co_{52}$ and $Pt_{76}Co_{24}$ catalysts locate at the peak positions, respectively. For comparison, the $Pt_{76}Co_{24}$ catalyst exhibits the best ORR performance with the lowest onset potential (−0.09 V) and highest electron transfer numbers (3.99), which is higher than that of the commercial Pt/C (E-TEK). The ORR kinetics enhancements are explained based on modification of the electronic characteristics of catalysts, based on the Pt 4f binding energy in this Pt–Co alloy series. It is evident that a counterbalance between two opposite effects that are related to the surface adsorption of active oxygen and oxygenate intermediates like OH can substantially improve electrochemical specific area of the catalysts, and thus enhance the ORR activity accordingly. The findings provide new insights into the synergistic catalytic activity for the design of Pt-based bimetallic electrocatalysts. This information is important for the understanding of the physical origin of the activity and selectivity of the Pt–Co alloy catalysts during the ORR.

Notes and references

State Key Laboratory of Chemical Resource Engineering, Beijing Key Laboratory of Electrochemical Process and Technology for Materials, Beijing University of Chemical Technology, Beijing 100029, China

*Corresponding author. Tel./fax: +8610 64411301.
E-mail address: liujingjun@mail.buct.edu.cn
**Corresponding author. Tel./fax: +8610 64451996.
E-mail address: wangf@mail.buct.edu.cn

1 Z. Duan and G. Wang, *The Journal of Physical Chemistry C*, 2013, 117, 6284–6292.

2 Y. Chen, Z. Liang, F. Yang, Y. Liu and S. Chen, *The Journal of Physical Chemistry C*, 2011, 115, 24073–24079.

3 N. Wakabayashi, M. Takeichi, H. Uchida and M. Watanabe, *The Journal of Physical Chemistry B*, 2005, 109, 5836–5841.

4 C. Wang, M. Chi, D. Li, D. van der Vliet, G. Wang, Q. Lin, J. F. Mitchell, K. L. More, N. M. Markovic and V. R. Stamenkovic, *ACS Catalysis*, 2011, 1, 1355–1359.

5 J. Greeley, I. Stephens, A. Bondarenko, T. P. Johansson, H. A. Hansen, T. Jaramillo, J. Rossmeisl, I. Chorkendorff and J. K. Nørskov, *Nature Chemistry*, 2009, 1, 552–556.

6 S. K. Meher and G. R. Rao, *The Journal of Physical Chemistry C*, 2013, 117, 4888–4900.

7 K.-S. Lee, T.-Y. Jeon, S. J. Yoo, I.-S. Park, Y.-H. Cho, S. H. Kang, K. H. Choi and Y.-E. Sung, *Applied Catalysis B: Environmental*, 2011, 102, 334–342.

8 C. Koenigsmann, M. E. Scofield, H. Liu and S. S. Wong, *The Journal of Physical Chemistry Letters*, 2012, 3, 3385–3398.

9 D. Mott, J. Luo, P. N. Njoki, Y. Lin, L. Wang and C.-J. Zhong, *Catalysis today*, 2007, 122, 378–385.

10 C. Bock, C. Paquet, M Couillard, G. A. Botton, and B. R. Mac Dougall, *Journal of the American Chemical Society*, 2004, 126 , 8028–8037.

11 H. Chen, D. Wang, Y. Yu, K. A. Newton, D. A. Muller, H.Abruña, and F. J. DiSalvo, *Journal of the American Chemical Society*, 2012, 134 , 18453–18459.

12 H. Schulenburg, E. Muller, G. Khelashvili, T. Roser, H. Bonnemann, A. Wokaun, G. G. Scherer, *The Journal of Physical Chemistry C,* 2009, 113, 4069-4077.

13 B. Lim, M. Jiang, P. H. C. Camargo, E. C. Cho, J. Tao, X. Lu, Y. Zhu, Y. Xia, *Science,* 2009, 324, 1302-1305.

14 V. R. Stamenkovic, B. S. Mun, M. Arenz, K. J. J. Mayrhofer, C. A. Lucas, G. Wang, P. N. Ross, N. M. Markovic, *Nature Materials,* 2007, 6, 241-247.

15 J. Luo, P. N. Njoki, Y. Lin, L. Wang, C. J. Zhong, *Electrochemistry Communications*, 2006, 8, 581-587.

16 Z. Sun, J. Masa, W. Xia, D. Konig, A. Ludwig, Z.-A. Li, M. Farle, W. Schuhmann and M. Muhler, *ACS Catalysis*, 2012, 2, 1647–1653.

17 P. Wu, P. Zhang, Y. Qian, Y. Hu, H. Zhang and C. Cai, *The Journal of Physical Chemistry C*, 2013, 117, 19091–19100.

18 B. Hammer and J. K. Nørskov, *Advances in catalysis*, 2000, 45, 71–129.

19 B. Lim, M. Jiang, P. H. Camargo, E. C. Cho, J. Tao, X. Lu, Y. Zhu and Y. Xia, *Science*, 2009, 324, 1302–1305.

20 K. A. Kuttiyiel, K. Sasaki, Y. Choi, D. Su, P. Liu and R. R. Adzic, *Nano letters*, 2012, 12, 6266–6271.

21 J. Du, Y. Pan, T. Zhang, X. Han, F. Cheng and J. Chen, *Journal of Materials Chemistry*, 2012, 22, 15812–15818.

22 L. Colmenares, Z. Jusys and R. Behm, *Langmuir*, 2006, 22, 10437–10445.

23 B. Blizanac, P. Ross and N. Markovic, *The Journal of Physical Chemistry B*, 2006, 110, 4735–4741.

This journal is © The Royal Society of Chemistry 2014

Phys. Chem. Chem. Phys., 2014, **00**, 1-3 | **9**

24   V. Stamenkovic, T. Schmidt, P. Ross and N. Markovic, *The Journal of Physical Chemistry B*, 2002, 106, 11970–11979.

25   J. Xu, P. Gao and T. Zhao, *Energy & Environmental Science*, 2012, 5, 5333–5339.

26   J. Wu, J. Zhang, Z. Peng, S. Yang, F. T. Wagner and H. Yang, *Journal of the American Chemical Society*, 2010, 132, 4984–4985.